



Article

# Sulfidation of ZIF-Derived Core-Shell NiCo LDH/Ni MOF Heterostructure toward Supercapacitor Electrodes with Enhanced Performance

Xin Zheng <sup>1,2,\*</sup>, <sup>†</sup> Yihui Sun <sup>3,†</sup>, Sijia Jin <sup>1</sup>, Minxuan Xu <sup>1</sup>, Yanyan Ding <sup>1</sup>, Fei Chen <sup>1</sup>, Tao Yang <sup>1</sup>, Qi Zhang <sup>1</sup>, Xinyue Zheng <sup>2</sup> and Hao Chen <sup>2,\*</sup>

<sup>1</sup> Center for Advanced Optoelectronic Materials, College of Materials and Environmental Engineering, Hangzhou Dianzi University, Hangzhou 310018, China

<sup>2</sup> College of Chemistry and Materials Engineering, Zhejiang A&F University, Hangzhou 311300, China

<sup>3</sup> Zhejiang Hikstor Technology Co., Ltd., Hangzhou 311300, China

\* Correspondence: vencen@hdu.edu.cn (X.Z.); haochen@zafu.edu.cn (H.C.)

† These authors contributed equally to this work.

**Abstract:** Developing electrodes in a reasonable structure is essential to boost the performance of supercapacitors. Self-supporting heterostructures enriched active sites are promising as binder-free electrodes for supercapacitors. Here, core-shell layered double hydroxide (LDH)/Metal organic frame (MOF) heterostructure was directly grown on carbon cloth (CC) substrate derived from L-Co ZIF NWAs. Subsequently, the composite was treated with a sulfidation process to optimize its electrical conductivity. Thanks to its unique network structure, it facilitates active site exposure and efficient charge transfer, together with the synergetic effect between NiCo double hydroxide and Ni MOF nanosheets. This hybrid electrode possesses an excellent specific capacity ( $1200 \text{ F g}^{-1}$  at  $1 \text{ A g}^{-1}$ ) and stable cycle performance with 86% capacity maintained after 4000 cycles, indicating its potential superiority for use in high-efficiency electrochemical capacitors.

**Keywords:** MOF; NiCo LDH; core-shell; sulfidation; supercapacitor



**Citation:** Zheng, X.; Sun, Y.; Jin, S.; Xu, M.; Ding, Y.; Chen, F.; Yang, T.; Zhang, Q.; Zheng, X.; Chen, H. Sulfidation of ZIF-Derived Core-Shell NiCo LDH/Ni MOF Heterostructure toward Supercapacitor Electrodes with Enhanced Performance. *Batteries* **2022**, *8*, 241. <https://doi.org/10.3390/batteries8110241>

Academic Editors: Liubing Dong and Zhengze Pan

Received: 14 September 2022

Accepted: 10 November 2022

Published: 15 November 2022

**Publisher's Note:** MDPI stays neutral with regard to jurisdictional claims in published maps and institutional affiliations.



**Copyright:** © 2022 by the authors. Licensee MDPI, Basel, Switzerland. This article is an open access article distributed under the terms and conditions of the Creative Commons Attribution (CC BY) license (<https://creativecommons.org/licenses/by/4.0/>).

## 1. Introduction

Because of environmental pollution and the energy crisis, it is urgent to develop a highly efficient and environmentally friendly energy storage/conversion system [1]. As opposed to conventional dielectric capacitors, supercapacitors can store dozens of times more energy, as well as deliver many times the power density of conventional batteries via longer life and greater reversibility [2], inspiring considerable research activities [3–5]. Electrode materials play a crucial role in the energy storage capability of SCs. Transition metal oxides and hydroxides, along with their derivatives, are considered promising electrode materials for supercapacitors because of their plentiful supply, specific redox behavior, low cost, and environmental benefits. 2D transition metal-based layered double hydroxides (LDH) with the unique two-dimensional planar channel, adjustable variability, low cost, and high stability have been claimed to be suitable for supercapacitors as electrode materials [6,7]. Nevertheless, the practical applicability of the LDH in supercapacitors is severely limited because of its sluggish electrical kinetics and facile agglomeration.

A reasonable structure offering active sites and promoting electron/ion transport is critical for efficient electron storage. Preparing target products by sacrificing MOFs as precursors and porous templates seems a promising approach for freestanding transition metal layered double hydroxides (TMLDH) array electrodes [8–11], which has been widely spread in a variety of fields [12–14]. The layering of double hydroxides (LDHs) provides charge-balancing anions at the interlayer between the layers, resulting in delamination and restacking. Additionally, LDH nanosheets with layered structures derived from MOF

would be superior for supercapacitors [15–17]. The core-shell design with the different components could not only increase the number of electrochemical reaction sites but also let different components contribute to mutual benefits [18–22]. For example, Feng Hao Hsu et al. [23] synthesized CoMoO<sub>4</sub>@NiWO<sub>4</sub> nanosheet core-shell arrays on Ni foam, and electrochemical properties of excellent quality were attained. Consequently, designing core-shell freestanding electrodes is still an area of active research for good electrochemical properties and incets many studies [24]. Ionized sulfur can prevent the structure from disintegrating via interlayer elongation, while LDH nanosheets with highly hydroxylated surfaces can improve their ability to absorb electrolytes [25]. Rough surfaces of ultrathin core-shell hybrid structures and sulfidation treatment of the hybrid array are expected to enhance active site exposure and electrolyte access [26].

Motivated by the above-mentioned and further improving the properties, herein, a freestanding electrode was constructed by growing ZIF-MOF arrays on the CC substrate. A triangle-shaped NiCo LDH was obtained via template evolution after alternate soaks. After the deposition of Ni MOF and further sulfidation treatment, the core-shell NiCo LDH/S-Ni MOF was finally constructed. The NiCo LDH core constructed a connective skeleton enhancing the wetting ability of sulfurized Ni MOF (S-Ni MOF) nanosheets to the electrolyte, and the S-Ni MOF shell with a large specific surface area offers many possible electrochemical reaction sites. Eliminating the binder from the freestanding arrays resulted in a reduction in electrical resistance and an increase in electron transport to the collector. In addition to providing more channels for ion and electrolyte transport, the formed core-shell structure could also release structural stresses during electrochemical reactions. Gaining from the core-shell hierarchical structure and sulfidation treatment, numerous electroactive sites, as well as synergistic effects between the components, the resulting NiCo-LDH/S-Ni MOF arrays electrode displayed excellent electrochemical performance, including a high specific capacitance of 1200 F g<sup>-1</sup> at a current density of 1 A g<sup>-1</sup>, and long cycling life (the capacitor retains 86% of its capacitance after 4000 cycles at 5 A g<sup>-1</sup>).

## 2. Materials and Methods

### 2.1. Synthesis of NiCo-LDH/S-Ni MOF

The carbon cloth (1.5 cm × 1 cm) was activated in a 3 M hydrochloric acid solution by ultrasonic for 25 min, then repeatedly washed with deionized water and ethanol and dried to constant weight. A 40 mmol cobalt nitrate hexahydrate (Co(NO<sub>3</sub>)<sub>2</sub> 6H<sub>2</sub>O) and a 40 mmol 2-methylimidazole (Hmim) aqueous solution were prepared. Immersing carbon cloth pieces into 24 mL of 2-methylimidazole (Hmim) aqueous solution and dropping 3 mL of cobalt nitrate aqueous solution at magnetic stirring for 10 min, and 2 h standby time was allowed for the reaction. After being washed with ethanol and deionized water, the CC@ZIF-67 products were dried at 50 °C [27]. Afterward, CC@ZIF-67 was alternately impregnated with 10 mmol nickel nitrate hexahydrate (Ni(NO<sub>3</sub>)<sub>2</sub> 6H<sub>2</sub>O) and 10 mmol cobalt nitrate hexahydrate for 24 h at room temperature. The samples were then washed three times with ethanol and dried at 50 °C. NiCo LDH/Ni MOF core shells were synthesized by the *in situ* growth of Ni MOF on NiCo LDH using the hydrothermal method. First, we mixed 1 mmol Ni(NO<sub>3</sub>)<sub>2</sub>·6H<sub>2</sub>O methanol solution (20 mL) with 4 mmol 2-methylimidazole (Hmim) methanol solution. Following magnetic stirring for 30 min, the CC@ NiCo LDH was immersed in the mixture at 120 °C for 24 h. After cooling, the product was washed repeatedly with methanol. Finally, it was dried overnight in a vacuum at 80 °C. Generally, NiCo LDH/Ni MOF products were suspended in 40 mL of ethanol for 20 min. A further 30 min of stirring was then performed by adding 0.4 g of thiourea. This was then transferred into a Teflon container with heat treatment of 160 °C for 3 h. The cooled product was filtered and repeatedly washed in ethanol after cooling. Lastly, a vacuum dryer was used to dry it overnight at 80 °C. After weighing the resulting electrodes and comparing them with the substrates, the mass loading of active materials was 2 mg cm<sup>-2</sup>.

## 2.2. Characterization and Measurements

To observe the samples under scanning electron microscopy, samples were cut to size and attached to an aluminum table with conductive adhesive. After ultrasonic dispersion, core-shell nano products of NiCo LDH/S-Ni MOF were removed from carbon cloth. For TEM and F20 transmission electron microscopy (FEI, Hillsboro, OR, USA) characterization, the alcohol solution with NiCo LDH/S-Ni MOF samples was applied to a copper net with a support film. The structure and element properties were evaluated using *in situ* energy dispersive spectroscopy (EDS). EOL-JSM-IT300HR field emission SEM (Japan Electronics, Okohama, Janpan) was used to take scanning electron microscopy (SEM) images. A Cu K $\alpha$  (40 kV, 30 mA,  $\lambda = 1.5418 \text{ \AA}$ ) D/max 2500 X-ray diffractometer (Rigaku, Tokyo, Janpan) was used with a scan rate of  $10^\circ \text{ min}^{-1}$  where XRD patterns in the  $2\theta$  range from 10 to  $80^\circ$ . A Ka-XPS X-ray photoelectron spectrometer (Thermo Scientific, Waltham, MA, USA) was used to measure X-ray photoelectron spectra. To correct the binding energy, we used the peak of C 1 s at 284.6 eV. BET surface area was measured using a ASAP 2460 instrument (Micromeritics, Norcross, GA, USA) with liquid nitrogen at 77.3 K.

## 2.3. Electrochemical Measurements

All electrochemical measurements were conducted using the CHI 660D (Chenhua, Shanghai, China) in a 1.0 M KOH aqueous solution. Samples were cut into  $1 \times 1 \text{ cm}^2$  squares and directly used as working electrodes. Pt plates were utilized as reference electrodes, and Hg/HgO electrodes served as counter electrodes. Following the galvanostatic charge-discharge (GCD) curves could be used to calculate the specific capacitance:  $C = It/mV$ , where I, t, m, and V represent the current (A), discharge rate (s), active mass loading (g), and potential window (V) of each cell, respectively. And a 5 mV signal was applied to an open-circuit voltage of 0.01 Hz to 100 kHz for electrochemical impedance spectroscopy (EIS).

## 3. Results

The synthetic route of NiCo LDH/S-Ni MOF core-shell hybrids is schematically depicted in Figure 1a. Firstly, NiCo LDH nanosheets were directly grown on carbon cloth by sacrificing triangle-shaped ZIF-67 templates. Then, a Ni-MOF shell was synthesized on the surface of NiCo LDH, developing a core-shell nanorod array electrode by a facile hydrothermal reaction. At last, the core-shell CC@NiCo LDH/Ni MOF was thermally sulfurized to give CC@NiCo LDH/S-Ni MOF in thiourea ethanol at  $160^\circ \text{C}$  for 3 h, which will improve electrolyte exposure and electrolyte accessibility. A sulfur ion can prevent corrosion in a structure by delaying the disintegration of the structure through layer elongation. Three samples were analyzed by SEM to show their morphologies (see Figure 1b–d). It appeared that all samples were sheet-like and grown continuously on carbon cloth substrates. NiCo LDH nanosheets derived from ZIF-67 exhibited uniform dispersion, indicating that ZIF-67-induced growth is beneficial for preventing the aggregation of 2D NiCo LDH. After introducing sulfurized Ni MOF, the S-Ni MOF nanosheets around the NiCo LDH nanosheets uniformly filled the space in between, which can effectively favor electrolyte penetration and electronic transmission and offer more active sites.

Further characterization of the as-prepared CC/NiCo LDH/S-Ni MOF hybrids was undertaken using TEM, as shown in Figure 2a–c. It demonstrated the NiCo LDH nanosheet feature, which accorded with the SEM observation. The Ni-Co LDH core was fully covered by the S-Ni MOF shell, and all exhibited a nanosheet-like structure. The sheet-like structure of S-Ni MOF was further confirmed by the image in Figure 2b, which demonstrates the existence of particles on the surface of Ni MOF. Figure 2c shows additional information about TEM (HRTEM) with a  $\text{Ni}_3\text{S}_2$  (101) plane spacing of 0.42 nm [28]. EDS (energy dispersive spectroscopy) is also available for the existence of the relevant elements of Ni, Co, S, C, and O. The results agree with the HRTEM, proving the success of the NiCo LDH/S-Ni MOF synthesized on CC. From the BET surface area curves (Figure S2), the surface area of the CC/NiCo LDH/S-Ni MOF is about  $5.2752 \text{ m}^2/\text{g}$ ; the surface area has been greatly improved compared with CC/NiCo LDH.

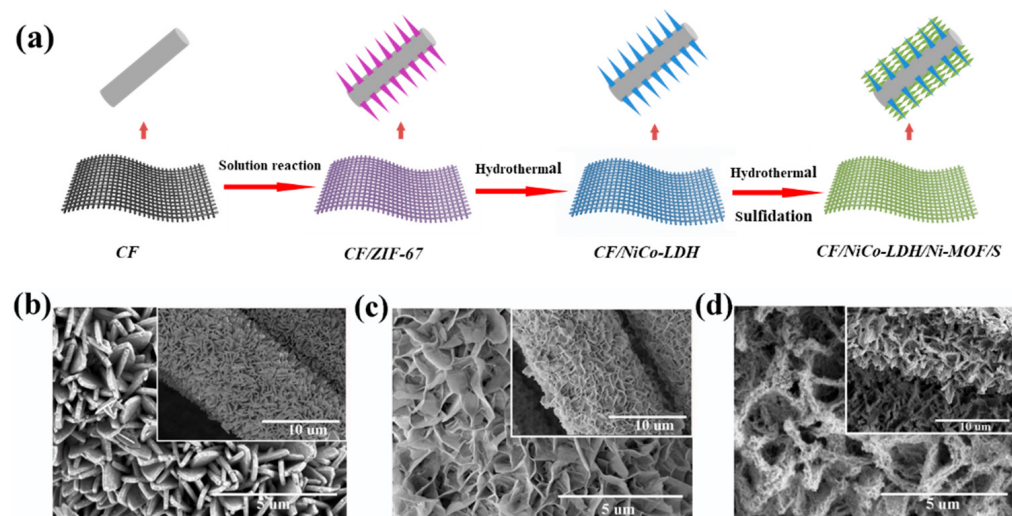


**Figure 1.** (a) Diagram illustrating the fabrication process of CC/NiCo LDH/S-Ni MOF electrode on carbon cloth, (b–d) Different magnification FESEM images of CC/Ni-Co LDH (b), CC/NiCo LDH/Ni MOF (c), and CC/NiCo LDH/S-Ni MOF (d).

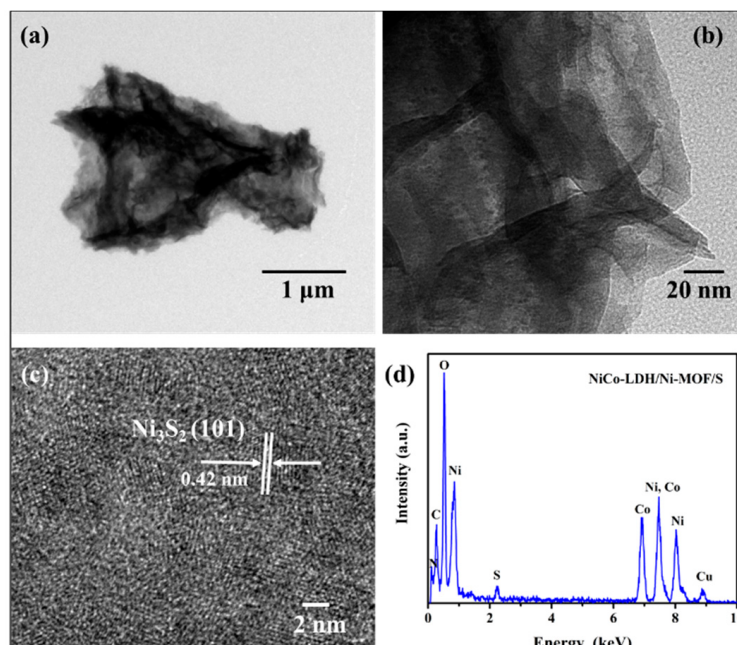


**Figure 2.** (a) Low magnification TEM images of CC/NiCo LDH/S-Ni MOF, (b) high-resolution TEM (HRTEM) image, (c) HRTEM image of the crystalline region, (d) The EDS spectrum of the CC/NiCo LDH/S-Ni MOF product.

XRD measurements were conducted to analyze the composition and phase of the obtained materials (see Figure 3a). Corresponding XRD patterns from CC/NiCo LDH/Ni MOF to CC/NiCo LDH/S-Ni MOF composites were observed and fitted. One typical broad and strong peak at  $2\theta$  of  $25^\circ$  was assigned to CC. As for the XRD patterns of Ni-Co LDH/Ni MOF, peaks of diffraction located at  $2\theta$  values of  $34.9^\circ$ ,  $43.8^\circ$ , and  $60.2^\circ$ , which can be indexed to (012), (015), and (110) plane reflections of NiCo LDH phase and a characteristic peak at  $11.2^\circ$  that denotes the crystal structure of Ni MOF [29,30]. After sulfidation of the NiCo LDH/Ni MOF heterostructure, the new diffraction peaks at  $21.5^\circ$  can be identified as (101) phases of Ni<sub>3</sub>S<sub>2</sub> (JCPDS 44-1418) [13], which is associated with TEM results. Notably, a peak signal of Ni MOF still exists after sulfidation due to the incomplete vulcanization of Ni MOF. Figure 3b,c illustrates how Ni, Co, O, and S are distributed among the NiCo

LDH/S-Ni MOF. It further provides evidence that NiCo LDH/S-Ni MOF core-shell sheets were successfully prepared.

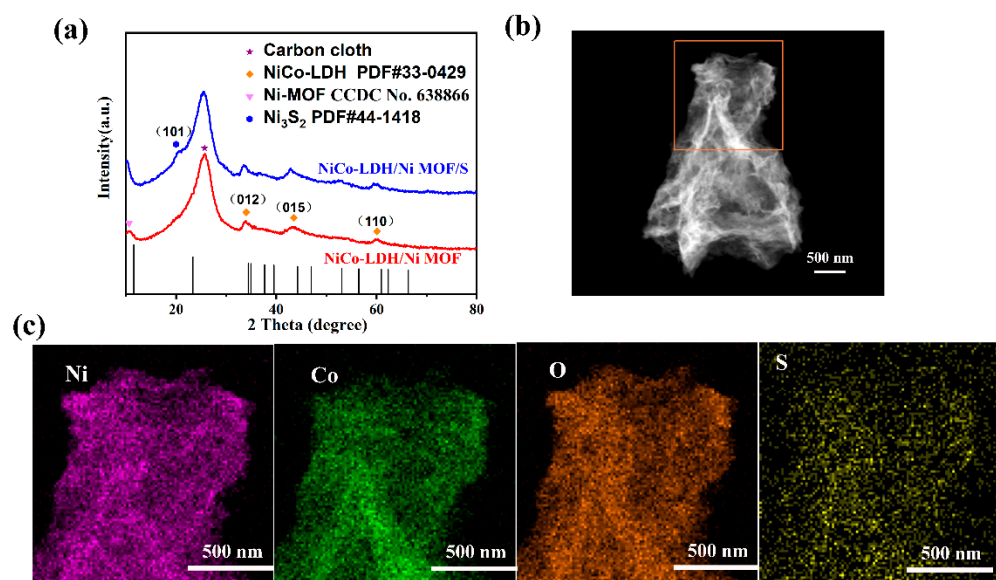
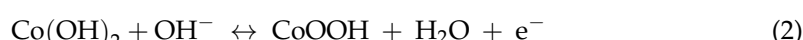
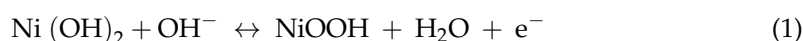


**Figure 3.** (a) XRD patterns of NiCo LDH/Ni MOF and NiCo LDH/S-Ni MOF (b,c) EDS mapping of NiCo LDH/S-Ni MOF samples.

An XPS survey of the NiCo LDH/S-Ni MOF samples was employed to confirm composition and valence (Figure 4). Consequently, Ni, Co, C, and S were present. In the XPS analysis of Ni 2p at high resolution (Figure 4a), two around 873.4 and 855.8 eV were the characteristic peaks of Ni<sup>2+</sup>. Between these two characteristics, 17.6 eV separated them. Two satellite peaks at 879.5 and 861.8 eV further confirmed the presence of Ni<sup>2+</sup> in the electrode material. In the high-resolution Co 2p spectra (Figure 4b), peaks at 799.4 eV (2p<sub>1/2</sub>) and 784 eV (2p<sub>3/2</sub>) could be typically indexed to Co<sup>2+</sup> state, while the peak for Co<sup>3+</sup> 2p<sub>3/2</sub> and 2p<sub>1/2</sub> presented at 781.0 eV and 796.3 eV with weak satellite peaks at 802.9 eV and 785.7 eV. It revealed the presence of Co (II) and Co (III) [31]. According to Figure 4c, the C1s spectrum shows two peaks at 284.8 and 286.5, which correspond to sp<sup>2</sup> carbon (C-C) and sp<sup>3</sup> carbon (C-O), respectively [32]. For S2p XPS, a weak peak at 164.4 eV is attributed to satellite peaks. Also, the highly oxidized surface sulfur at 169.2 eV accounted for the strong peak [33]. The other peak at approximately 170.28 eV was also observed in the spectrum, suggesting that S is bound to metals since previous studies have shown that S 2p binding energy peaks shifts higher when S is bound to metals [34]. Such a heterostructure composite jointed redox states for the Co and Ni species, particularly those resulting from the sulfidation treatment, is valuable for intrinsic faradaic activity.

A three-electrode system was used to examine electrode materials to evaluate their electrochemical performance. Figure 5a indicates comparison curves for the CV of the NiCo LDH, NiCo LDH/Ni MOF, and NiCo LDH/S-Ni MOF at 2 mV s<sup>-1</sup> between -0.2 V and 0.5 V, and the oxidation and reduction peaks can be identified at around 0.35 V and 0.2 V, respectively. Additionally, according to the literature [35], the redox peak potentials vs. Hg/HgO of Ni(OH)<sub>2</sub> are 0.49 V and 0.36 V while those of Co (OH)<sub>2</sub> are respectively 0.57 V and 0.47 V, so the capacitive properties are jointly contributed and primarily dominated by the faradic reactions of Ni<sup>2+</sup> and Co<sup>2+</sup>. Chemical reaction equations corresponding to the redox peaks are listed below:



As can be seen, from NiCo LDH to NiCo LDH/S-Ni MOF, the response current and the areas surrounded by the CV curve increased at the same scan rate of  $2 \text{ mV s}^{-1}$ , indicating a higher specific capacitance can be obtained by sulfide treatment. The carbon cloth substrate contributed little to the electrochemical performance, which can be proved by the CV curves of the carbon cloth substrate (see Figure S1 of Supplementary Materials). The GCD data of the three electrodes were compared in Figure 5b. Galvanostatic charge-discharge measurements were subsequently tested to estimate the specific capacitance. It turned out that NiCo LDH/S-Ni MOF hybrid electrodes possess a longer discharge time at the same discharge current compared with other electrodes, indicating a higher level of stored charge and better electrochemical behavior. Thus, NiCo LDH/S-Ni MOF was selected as the most appropriate electrode material for the next electrochemical measurements. The CV curves of the NiCo LDH/S-Ni MOF sample at different scan rates are indicated in Figure S4 of Supplementary Materials. According to the GCD curves shown in Figure 5c, the voltage plateaus indicate redox reactions occur in electrochemical processes, consistent with CV characterizations. The specific capacitances of NiCo LDH, NiCo LDH/S-Ni MOF, and NiCo LDH/S-Ni MOF at various current densities are calculated and depicted in Figure 5d. When the current density was increased from 1 to  $10 \text{ A g}^{-1}$ , the specified capacitances of NiCo LDH/S-Ni MOF, NiCo LDH/Ni MOF, and pure NiCo LDH decreased from  $1200, 840, 690 \text{ F g}^{-1}$  to  $810, 478, 290 \text{ F g}^{-1}$ , respectively. We compared the electrochemical performance of NiCo LDH/S-Ni MOF with some relevant materials reported in the literature [18,27,36–40]. The specific capacitance of the NiCo LDH/S-Ni MOF ( $1200 \text{ F/g}$ ) was considerably higher than that of Ni/Ni<sub>3</sub>S<sub>2</sub>/CNFs ( $704 \text{ F/g}$ ) [38], Ni/Co-MOF-rGO ( $860 \text{ F/g}$ ) [18], Co(OH)<sub>2</sub>/Ni-Co LDH ( $825.6 \text{ F/g}$ ) [39], Ni-Co LDH/3D RGO ( $1054 \text{ F/g}$ ) [40], and NiCo-MOF@PNTs ( $1109 \text{ F/g}$ ) [27], indicating that NiCo LDH/S-Ni MOF electrodes are promising electrodes for high-efficiency supercapacitors. Importantly, the NiCo LDH/S-Ni MOF electrode materials exhibited a good capability rate retaining 67.5% of the original capacitance, probably due to a hybrid structure and distinct hierarchy.

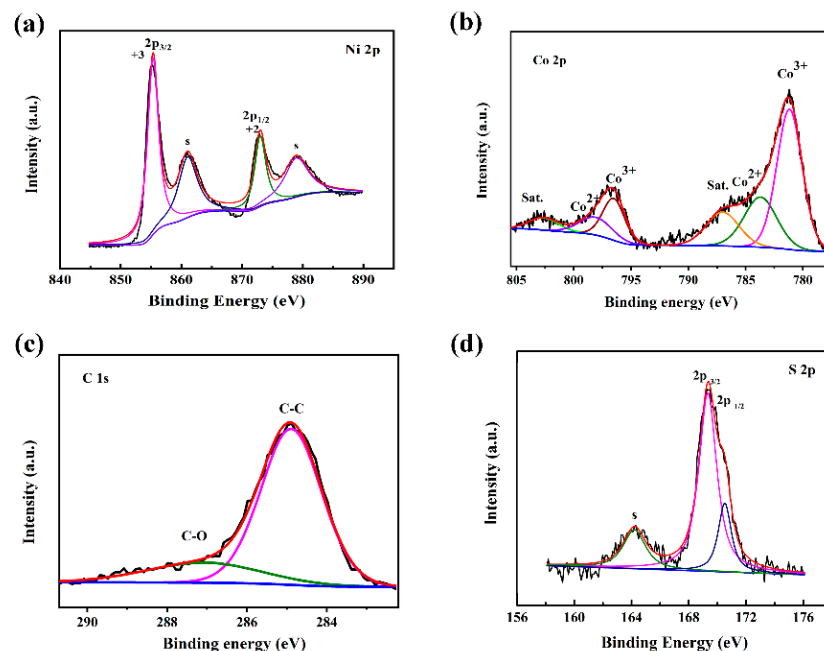


**Figure 4.** XPS wide spectrum (a) Ni 2p (b) Co 2p (c) C 1s (d) S 2p. The color curves are peak fitting curves.

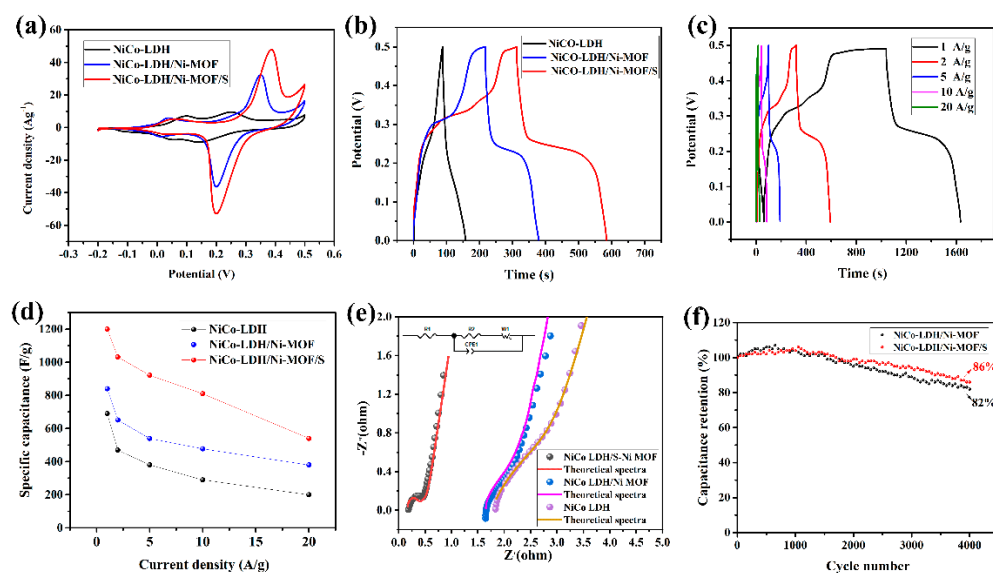


**Figure 5.** (a) comparison of CV curves of NiCo LDH, NiCo LDH/Ni MOF, and NiCo LDH/S-Ni MOF at  $2 \text{ mV s}^{-1}$ ; (b) Galvanostatic discharge curves of NiCo LDH, NiCo LDH/Ni MOF, and NiCo LDH/S-Ni MOF sample at a current density of  $2 \text{ A g}^{-1}$ ; (c) corresponding GCD curves of NiCo LDH/S-Ni MOF at different current density; (d) capacitance of NiCo LDH, NiCo LDH/S-Ni MOF, and NiCo LDH/S-Ni MOF electrodes at different current density; (e) Nyquist plots of Ni-Co LDH, NiCo LDH/Ni MOF and NiCo LDH/S-Ni MOF; (f) cycling stability comparison of NiCo LDH/Ni MOF electrodes and NiCo LDH/S-Ni MOF electrodes at the current density of  $5 \text{ A g}^{-1}$ .

The reaction kinetics and capacitive behavior of the device were further tested by EIS measurements, as seen in Figure 5e. All spectra were composed of a typical semicircle in the high-frequency region and a straight line at low frequency. The diameter of the semicircle corresponded to the charge-transfer resistance ( $R_{\text{ct}}$ ) of the electrode. The  $R_{\text{ct}}$  values for CC/NiCo LDH, CC/NiCo LDH/Ni MOF, and CC/NiCo LDH/S-Ni MOF were calculated as  $2.53 \Omega$ ,  $1.91 \Omega$ , and  $0.16 \Omega$ , respectively. The charge-transfer resistance ( $R_{\text{ct}}$ ) decreased obviously after sulphurization. The straight line at the low-frequency regime represents the Warburg region, related to the diffusion of electrolyte ions to the reaction interface. The larger angle to the virtual  $Z'$  axis from the low-frequency region reflected the reduced diffusion path length of electrolyte ions. NiCo LDH/S-Ni MOF curves exhibited a phase angle exceeding  $60^\circ$  at low frequency, indicating an increased diffusion and migration rate of electrolyte ions. Furthermore, a four-electrode probe method was used to analyze the intrinsic electrical conductivity of Ni-Co LDH, NiCo LDH/Ni MOF, and NiCo LDH/S-Ni MOF samples. The conductivity of the NiCo LDH/S-Ni MOF sample was about  $6.95 \text{ S/cm}$ , with  $35.3\%$  enhancement compared to Ni-Co LDH. These results indicated that sulfurization treatment increases conductivity and facilitates the ion intercalation process. Another important parameter is cycle stability. In Figure 5f, the cycling stability values of the three-electrode types are presented at a current density of  $5 \text{ A g}^{-1}$ . After a 4000 cycles charge-discharge process, the NiCo LDH/S-Ni MOF electrode retained about  $86\%$  original capacitance, better than the NiCo LDH/Ni MOF electrode ( $82\%$ ). The coulombic efficiency maintained about  $99\%$  during 4000 cycles (Figure S8). The Nyquist plots before and after 4000 GCD cycles showed an increase in the  $R_{\text{ct}}$  values and a slight decrease in the slope for the straight line after 4000 GCD cycles Figure S6. The morphology did not change greatly; only parts of the SEM structures collapsed after 4000 cycling (Figure S7), further indicating high cycling stability and a good reversible redox reaction of the CC/NiCo LDH/S-Ni MOF, owing to the fact that sulfur ions can prevent the structure from disintegrating by elongating between layers. A small capacitance increase can be seen before the initial cycles. This may have resulted from an activation process during the start of the test. Increasingly, more electrode material is activated as the electrolyte penetrates the electrode, contributing

to an increase in specific capacitance. Later on, the capacitance gradually decreased. The better cycling stabilities are due to the stable bonds stabilizing the framework and the highly reversible groups after sulfide treatment.

Interface/surface structure engineering is credited with excellent performance, including capacitance and cyclic stability. Figure 6 describes the schematic of electron and ion transport in the core-shell NiCo LDH/S-Ni MOF electrode structure. Structural tuning of core/shell heterostructure nanoarrays by the template-assisted method was used to optimize electrochemical performance [41,42]. By eliminating binders and conductors used in conventional processes, self-supporting electrodes removed the dead volume caused by dead volume. The large dimension of the sheets can ensure a high degree of mass utilization by reducing the risk of stacking or aggregation; 3D open networks provide large electrode-electrolyte interfaces, as well as plenty of electroactive sites. The sulfuretted Ni MOF nanosheets were elaborately introduced into the NiCo LDH nano scaffold to accelerate the ionic and electronic diffusion/transport kinetics. Sulfide treatment offers fast ion diffusion within sheets and reduces overall resistance. Through the elongation between the layers induced by sulfur ions, structure corrosion can be prevented and excellent stability can result. Remarkably, the strategy of constructing a reasonable interface/surface structure built from MOF templates may be applied to other electrochemical fields.

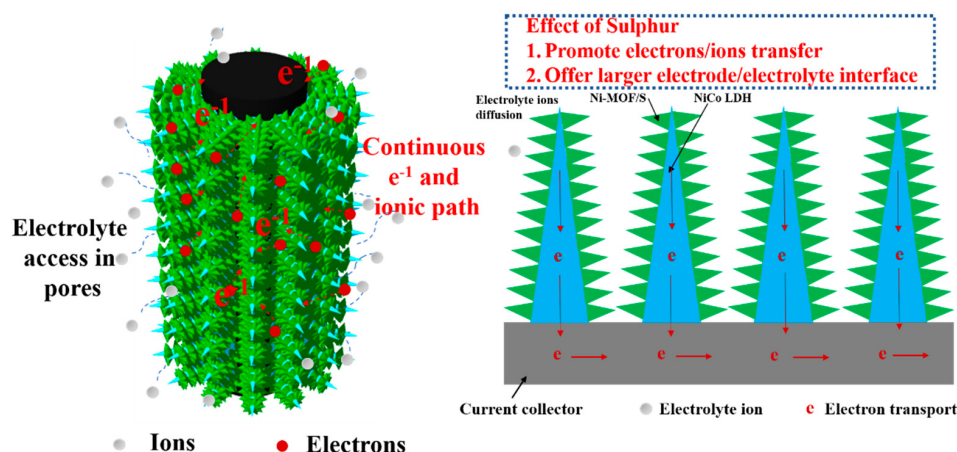


**Figure 6.** Schematic illustration of the electron and ion transport in the LDH/Ni-MOF/S electrode.

#### 4. Conclusions

In this paper, self-supporting NiCo LDH nanosheets were synthesized and derived from the sacrificial template of Co-based zeolitic imidazolate frameworks (ZIF-67). After that, S-Ni MOF was in situ electrodeposited, creating a core-shell structure, aiming for more active sites, fast ion diffusion, and stable structure. Benefiting from the synergistic effects between individual components, the LDH/S-Ni MOF electrode exhibited an optimal specific capacitance of  $1200 \text{ F g}^{-1}$  at  $1 \text{ A g}^{-1}$ . Compared to the LDH/Ni MOF electrodes without sulfide treatment, the capacitance improved by 32.5%, and excellent cycle stability with 86% capacity was maintained after 4000 cycles. In rational hybrids, a large amount of electrochemically active sites and fast ion diffusion accounts for better electrochemical performance. Consequently, our findings open possibilities for constructing freestanding hierarchical electrodes, which could be used in high-performance supercapacitors.

**Supplementary Materials:** The following supporting information can be downloaded at: <https://www.mdpi.com/article/10.3390/batteries8110241/s1>; Figure S1: CV curve of carbon cloth at 2 mV/s; Figure S2: BET surface area comparison; Figure S3: Conductivity of of Ni-Co LDH, NiCo LDH/Ni MOF, and NiCo LDH/S-Ni MOF sample; Figure S4: CV curves of the NiCo LDH/S-Ni MOF electrode at different scan rate of ranging from  $-0.2\text{--}0.5 \text{ V}$ ; Figure S5: Electrochemical properties comparison of the NiCo LDH/S-Ni MOF electrode material with some relevant materials reported previously; Figure S6: EIS comparison of NiCo LDH/S-Ni MOF sample before and after 4000 cycles;

Figure S7: (a,b) SEM images of NiCo LDH/S-Ni MOF sample before and after 4000 cycles; Figure S8: Coulombic efficiency at current density of  $5 \text{ Ag}^{-1}$ .

**Author Contributions:** X.Z. (Xin Zheng): Conceptualization, Project administration, Supervision, Writing—Review & Editing; Y.S.: Conceptualization, Methodology, Investigation, Data Curation, Formal analysis. S.J.: Data Curation, Visualization; M.X.: Resources, Investigation; Y.D.: Investigation, Validation; F.C.: Resources, Formal analysis; T.Y.: Formal analysis, Validation; Q.Z.: Visualization; X.Z. (Xinyue Zheng): Supply data for the revised manuscript; H.C.: Conceptualization, Supervision. All authors have read and agreed to the published version of the manuscript.

**Funding:** This work was supported by the National Nature Science Foundation of China (No. 52102230, 11847076, 52002101, 51872069), the Zhejiang Provincial Natural Science Foundation of China (No. LQ19E020005, LQ20E020007, LQ20E020006) and Scientific Research Project of Zhejiang Education Department (Grant No. Y201942097), Starting Foundation of Hangzhou Dianzi University (No. KYS205618042).

**Institutional Review Board Statement:** Not applicable.

**Informed Consent Statement:** Not applicable.

**Data Availability Statement:** Not applicable.

**Conflicts of Interest:** The authors declare no conflict of interest.

## References

1. Ma, M.; Yang, Y.; Chen, Y.; Jiang, J.; Ma, Y.; Wang, Z.; Huang, W.; Wang, S.; Liu, M.; Ma, D.; et al. Fabrication of hollow flower-like magnetic  $\text{Fe}_3\text{O}_4/\text{C}/\text{MnO}_2/\text{C}_3\text{N}_4$  composite with enhanced photocatalytic activity. *Sci. Rep.* **2021**, *11*, 2597–2608. [[CrossRef](#)]
2. Abdul Sammed, K.; Pan, L.; Farid, A.; Javid, M.; Yang, S.; Asif, M. Carbon Nanocoil-Supported Three-Dimensional Structure of Nickel–Cobalt Nitrides as the Electrode Material for Supercapacitors. *ACS Appl. Energy Mater.* **2021**, *4*, 6678–6687. [[CrossRef](#)]
3. Lonkar, S.P.; Pillai, V.V.; Patole, S.P.; Alhassan, S.M. Scalable In Situ Synthesis of 2D–2D-Type Graphene-Wrapped  $\text{SnS}_2$  Nano hybrids for Enhanced Supercapacitor and Electrocatalytic Applications. *ACS Appl. Energy Mater.* **2020**, *3*, 4995–5005. [[CrossRef](#)]
4. Kwon, Y.S.; Park, G.-T.; Lee, J.-S.; Hwang, G.-H.; Jeong, Y.G. Poly(Ether Amide)-Derived, Nitrogen Self-Doped, and Interfused Carbon Nanofibers as Free-Standing Supercapacitor Electrode Materials. *ACS Appl. Energy Mater.* **2021**, *4*, 1517–1526.
5. Mohammadi Zardkhoshouei, A.; Ameri, B.; Hosseini Davarani, S.S. A high-energy-density supercapacitor with multi-shelled nickel-manganese selenide hollow spheres as cathode and double-shell nickel-iron selenide hollow spheres as anode electrodes. *Nanoscale* **2021**, *13*, 2931–2945. [[CrossRef](#)] [[PubMed](#)]
6. Liu, Y.; Fu, N.; Zhang, G.; Xu, M.; Lu, W.; Zhou, L.; Huang, H. Design of Hierarchical  $\text{NiCo@NiCo}$  Layered Double Hydroxide Core–Shell Structured Nanotube Array for High-Performance Flexible All-Solid-State Battery-Type Supercapacitors. *Adv. Funct. Mater.* **2017**, *27*, 1605307. [[CrossRef](#)]
7. Ramachandran, R.; Lan, Y.; Xu, Z.-X.; Wang, F. Construction of NiCo-Layered Double Hydroxide Microspheres from Ni-MOFs for High-Performance Asymmetric Supercapacitors. *ACS Appl. Energy Mater.* **2020**, *3*, 6633–6643. [[CrossRef](#)]
8. Wang, J.; Tang, J.; Ding, B.; Chang, Z.; Hao, X.; Takei, T.; Kobayashi, N.; Bando, Y.; Zhang, X.; Yamauchi, Y. Self-Template-Directed Metal–Organic Frameworks Network and the Derived Honeycomb-Like Carbon Flakes via Confinement Pyrolysis. *Small* **2018**, *14*, 1704461. [[CrossRef](#)]
9. Li, S.; Shi, C.; Pan, Y.; Wang, Y. 2D/2D NiCo-MOFs/GO hybrid nanosheets for high-performance asymmetrical supercapacitor. *Diam. Relat. Mater.* **2021**, *115*, 108358. [[CrossRef](#)]
10. Zheng, D.; Wen, H.; Sun, X.; Guan, X.; Zhang, J.; Tian, W.; Feng, H.; Wang, H.; Yao, Y. Ultrathin Mn Doped Ni-MOF Nanosheet Array for Highly Capacitive and Stable Asymmetric Supercapacitor. *Chemistry* **2020**, *26*, 17149–17155. [[CrossRef](#)]
11. Yang, Q.; Wang, Q.; Long, Y.; Wang, F.; Wu, L.; Pan, J.; Han, J.; Lei, Y.; Shi, W.; Song, S. In Situ Formation of  $\text{Co}_9\text{S}_8$  Quantum Dots in MOF-Derived Ternary Metal Layered Double Hydroxide Nanoarrays for High-Performance Hybrid Supercapacitors. *Adv. Energy Mater.* **2020**, *10*, 1903193. [[CrossRef](#)]
12. Hu, B.; Shang, X.; Nie, P.; Zhang, B.; Xu, K.; Yang, J.; Qiu, J.; Liu, J. Facile Fabrication of a Highly Porous N-Doped Nanotubular Carbon Aerogel by an In Situ Template-Growth Method for High-Performance Supercapacitors. *ACS Appl. Energy Mater.* **2021**, *4*, 6991–7001. [[CrossRef](#)]
13. Xu, X.; Tang, J.; Qian, H.; Hou, S.; Bando, Y.; Hossain, M.S.A.; Pan, L.; Yamauchi, Y. Three-Dimensional Networked Metal–Organic Frameworks with Conductive Polypyrrole Tubes for Flexible Supercapacitors. *ACS Appl. Mater. Interfaces* **2017**, *9*, 38737–38744. [[CrossRef](#)] [[PubMed](#)]
14. Chen, C.; Zhao, M.; Cai, Y.; Zhao, G.; Xie, Y.; Zhang, L.; Zhu, G.; Pan, L. Scalable synthesis of strutted nitrogen doped hierarchical porous carbon nanosheets for supercapacitors with both high gravimetric and volumetric performances. *Carbon* **2021**, *179*, 458–468. [[CrossRef](#)]

15. Jin, H.; Yuan, D.; Zhu, S.; Zhu, X.; Zhu, J. Ni-Co layered double hydroxide on carbon nanorods and graphene nanoribbons derived from MOFs for supercapacitors. *Dalton. Trans.* **2018**, *47*, 8706–8715. [[CrossRef](#)]
16. Xuemin, Y.; Hejun, L.; Ruimei, Y.; Jinhua, L. NiCo LDH nanosheets grown on MOF-derived  $\text{Co}_3\text{O}_4$  triangle nanosheet arrays for high-performance supercapacitor. *J. Mater. Sci. Technol.* **2021**, *62*, 60–69. [[CrossRef](#)]
17. Tang, J.; Shen, Y.; Miao, X.; Qin, H.; Song, D.; Li, Y.; Qu, Y.; Yin, Z.; Ren, J.; Wang, L.; et al. Template-directed growth of hierarchically structured MOF-derived LDH cage hybrid arrays for supercapacitor electrode. *J. Electroanal. Chem.* **2019**, *840*, 174–181. [[CrossRef](#)]
18. Rahmanifar, M.S.; Hesari, H.; Noori, A.; Masoomi, M.Y.; Morsali, A.; Mousavi, M.F. A dual Ni/Co-MOF-reduced graphene oxide nanocomposite as a high performance supercapacitor electrode material. *Electrochim. Acta* **2018**, *275*, 76–86. [[CrossRef](#)]
19. Xie, T.; Xu, J.; Wang, J.; Xuan, C.; Ma, C.; Su, L.; Dong, F.; Gong, L. In Situ Growth of Core–Shell Heterostructure  $\text{CoMoO}_4@\text{CuCo}_2\text{S}_4$  Meshes as Advanced Electrodes for High-Performance Supercapacitors. *Energy Fuel* **2020**, *34*, 16791–16799. [[CrossRef](#)]
20. Ansarinejad, H.; Shabani-Nooshabadi, M.; Ghoreishi, S.M. Enhanced Supercapacitor Performance Using a  $\text{Co}_3\text{O}_4@\text{Co}_3\text{S}_4$  Nanocomposite on Reduced Graphene Oxide/Ni Foam Electrodes. *Chem. Asian J.* **2021**, *16*, 1258–1270. [[CrossRef](#)]
21. Xu, X.; Liu, Y.; Wang, M.; Zhu, C.; Lu, T.; Zhao, R.; Pan, L. Hierarchical hybrids with microporous carbon spheres decorated three-dimensional graphene frameworks for capacitive applications in supercapacitor and deionization. *Electrochim. Acta* **2016**, *193*, 88–95. [[CrossRef](#)]
22. Pan, J.; Wang, F.; Zhang, L.; Song, S.; Zhang, H. Clean synthesis of  $\text{ZnCo}_2\text{O}_4@\text{ZnCo-LDHs}$  yolk–shell nanospheres composed of ultra-thin nanosheets with enhanced electrocatalytic properties. *Inorg. Chem. Front.* **2019**, *6*, 220–225. [[CrossRef](#)]
23. Hsu, F.H.; Hsu, S.Y.; Pao, C.W.; Chen, J.L.; Chen, C.L.; Chen, J.M.; Lu, K.T. Electrochemical properties and mechanism of  $\text{CoMoO}_4@\text{NiWO}_4$  core-shell nanoplates for high-performance supercapacitor electrode application studied via in situ X-ray absorption spectroscopy. *Nanoscale* **2020**, *12*, 13388–13397. [[CrossRef](#)] [[PubMed](#)]
24. Wang, H.; Wang, J.; Liang, M.; He, Z.; Li, K.; Song, W.; Tian, S.; Duan, W.; Zhao, Y.; Miao, Z. Novel Dealloying-Fabricated NiS/NiO Nanoparticles with Superior Cycling Stability for Supercapacitors. *ACS Omega* **2021**, *6*, 17999–18007. [[CrossRef](#)] [[PubMed](#)]
25. Wu, L.L.; Wang, Q.S.; Li, J.; Long, Y.; Liu, Y.; Song, S.Y.; Zhang, H.J.  $\text{Co}_9\text{S}_8$  Nanoparticles-Embedded N/S-Codoped Carbon Nanofibers Derived from Metal-Organic Framework-Wrapped CdS Nanowires for Efficient Oxygen Evolution Reaction. *Small* **2018**, *14*, 1704035. [[CrossRef](#)]
26. Long, Y.-W.; Zeng, H.-Y.; Li, H.-B.; Zou, K.-M.; Xu, S.; Cao, X.-J. Sulfidation of CoAl-layered double hydroxide on Ni foam for high-performance supercapacitors. *Electrochim. Acta* **2020**, *361*, 137098. [[CrossRef](#)]
27. Zhang, J.; Xiao, K.; Zhang, T.; Qian, G.; Wang, Y.; Feng, Y. Porous nickel-cobalt layered double hydroxide nanoflake array derived from ZIF-L-Co nanoflake array for battery-type electrodes with enhanced energy storage performance. *Electrochim. Acta* **2017**, *226*, 113–120. [[CrossRef](#)]
28. Dhandapani, B.; Jagannathan, M.; AlSalhi, M.S.; Aljaafreh, M.J.; Prasad, S. N-doped carbon embedded  $\text{Ni}_3\text{S}_2$  electrocatalyst material towards efficient hydrogen evolution reaction in broad pH range. *Colloid Surface A* **2020**, *603*, 125194. [[CrossRef](#)]
29. Liang, H.Y.; Lin, J.H.; Jia, H.A.; Chen, S.L.; Qi, J.L.; Cao, J.; Lin, T.S.; Fei, W.D.; Feng, J.C. Hierarchical NiCo-LDH@ $\text{NiOOH}$  core-shell heterostructure on carbon fiber cloth as battery-like electrode for supercapacitor. *J. Power Sources* **2018**, *378*, 248–254. [[CrossRef](#)]
30. Li, F.L.; Wang, P.T.; Huang, X.Q.; David James, Y. Large-Scalable, Bottom-Up Synthesis of Binary Metal-Organic Framework Nanosheets for Efficient Water Oxidation. *Angew. Chem.* **2019**, *58*, 7051–7056. [[CrossRef](#)]
31. Chauhan, M.; Reddy, K.P.; Gopinath, C.S.; Deka, S. Copper Cobalt Sulfide Nanosheets Realizing a Promising Electrocatalytic Oxygen Evolution Reaction. *ACS Catal.* **2017**, *7*, 5871–5879. [[CrossRef](#)]
32. Tran, T.S.; Dutta, N.K.; Choudhury, N.R. Poly(ionic liquid)-Stabilized Graphene Nanoinks for Scalable 3D Printing of Graphene Aerogels. *ACS Appl. Nano Mater.* **2020**, *3*, 11608–11619. [[CrossRef](#)]
33. Guan, B.; Li, Y.; Yin, B.; Liu, K.; Wang, D.; Zhang, H.; Cheng, C. Synthesis of hierarchical NiS microflowers for high performance asymmetric supercapacitor. *Chem. Eng. J.* **2017**, *308*, 1165–1173. [[CrossRef](#)]
34. Zhou, S.; Chen, S.; Yuan, Y.; Lu, Q. Influence of Humic Acid Complexation with Metal Ions on Extracellular Electron Transfer Activity. *Sci. Rep.* **2015**, *5*, 17067. [[CrossRef](#)]
35. Xiong, H.; Liu, L.; Fang, L.; Wu, F.; Zhang, S.; Luo, H.; Tong, C.; Hu, B.; Zhou, M. 3D self-supporting heterostructure NiCo-LDH/ZnO/CC electrode for flexible high-performance supercapacitor. *J. Alloys Compd.* **2021**, *857*, 158275. [[CrossRef](#)]
36. Zhang, Y.-D.; Lin, B.-P.; Sun, Y.; Zhang, X.-Q.; Yang, H.; Wang, J.-C. Carbon nanotubes@metal–organic frameworks as Mn-based symmetrical supercapacitor electrodes for enhanced charge storage. *RSV Adv.* **2015**, *5*, 58100–58106. [[CrossRef](#)]
37. Ahmad, R.; Iqbal, N.; Noor, T. Development of ZIF-Derived Nanoporous Carbon and Cobalt Sulfide-Based Electrode Material for Supercapacitor. *Materials* **2019**, *12*, 29–40. [[CrossRef](#)]
38. Tian, D.; Chen, S.-H.; Zhu, W.-D.; Wang, D.; Lu, X.-F. Metal-organic framework derived hierarchical Ni/ $\text{Ni}_3\text{S}_2$  decorated carbon nanofibers for high-performance supercapacitors. *Mater. Chem. Front.* **2019**, *3*, 1653–1660. [[CrossRef](#)]
39. Zhou, Y.; Jiang, Y.; Hu, Z.; Lang, X. Preparation and Application of  $\text{Co}(\text{OH})_2/\text{Ni-Co LDH}$  as Electrodes in Supercapacitors. *Int. J. Electrochem. Sci.* **2019**, *14*, 539–541. [[CrossRef](#)]

40. Bai, X.; Liu, Q.; Zhang, H.-S.; Liu, J.-Y.; Li, Z.-S.; Jing, X.-Y.; Yuan, Y.; Liu, L.-H.; Wang, J. Nickel-Cobalt Layered Double Hydroxide Nanowires on Three Dimensional Graphene Nickel Foam for High Performance Asymmetric Supercapacitors. *Electrochim. Acta* **2016**, *215*, 492–499. [[CrossRef](#)]
41. Wang, D.; Cao, L.; Luo, D.; Gao, R.; Li, H.; Wang, D.; Sun, G.; Zhao, Z.; Li, N.; Zhang, Y.; et al. Chain mail heterostructured hydrangea-like binary metal sulfides for high efficiency sodium ion battery. *Nano Energy* **2021**, *87*, 106185. [[CrossRef](#)]
42. Zhang, Y.Y.; Chen, P.; Wang, Q.Y.; Wang, Q.; Zhu, K.; Ye, K.; Wang, G.L.; Cao, D.X.; Yan, J.; Zhang, Q. High-Capacity and Kinetically Accelerated Lithium Storage in MoO<sub>3</sub> Enabled by Oxygen Vacancies and Heterostructure. *Adv. Energy Mater.* **2021**, *7*, 2101712. [[CrossRef](#)]